PHYSICAL REVIEW FLUIDS **9**, 064701 (2024)

Editors' Suggestion

Impact of rotation change on the emptying of an ideal bottle of water

A. Caquas,[1,2] L. R. Pastur,[1] and A. Genty[2]

[1]*Unité de Mécanique, ENSTA Paris, Institut Polytechnique de Paris, Palaiseau F-91120, France*

[2]*Université Paris-Saclay, CEA, Service de Thermo-hydraulique et de Mécanique des Fluides, Gif-sur-Yvette F-91191, France*

(Received 17 January 2022; accepted 23 April 2024; published 4 June 2024)

We are carrying out the experimental study of the emptying of a hermetically sealed cylindrical tank in a rotating frame. We determine the optimal rotational velocity for the tank, which minimizes the emptying time. Moreover, there exists a critical rotation velocity at which the emptying time exceeds that of the nonrotating case, depending on the relative duration of each of the three emptying regimes identified in this flow, namely, (i) a bubble regime, (ii) a vortical air jet regime, and (iii) a bathtub vortex regime. The three regimes, easily distinguished by the shape of the air-water interface, have different draining velocities. The lifetime of each regime, as well as the transitions between them, depend on both the water level and the rotating velocity of the platform.

DOI: 10.1103/PhysRevFluids.9.064701

I. INTRODUCTION

About 400 years ago, Torricelli [1] formulated the law describing the emptying of a vessel. Since then, numerous studies have been conducted on free-surface tank draining, resulting in refined versions of Torricelli's law based on experimental findings and adapted to a wider range of configurations [2–5].

While the industrialization of glass bottles began contemporaneously with Torricelli's discovery, the emptying of bottles [6–9], sealed cylinders [10–16], and cubic tanks [17–19] was first studied only 35 years ago [20]. Many studies have investigated the emptying time of sealed tanks [6,7,10–13,20] and the influence of tank and outlet size and geometry [6,9–12,20], inclination [6,8,9,11,20], temperature [18,20], surface tension [9], and more recently on the influence of bottle perforation [21]. Furthermore, the periodic occurrence of bubbles during tank draining, which is commonly known as the "glug-glug" phenomenon, has been described and modeled in many works [13,14,17,22–24].

Spinning a bottle of water to empty it faster or creating a "tornado in a bottle" [25] are well known experiments to the general public. Vortices, which promote fluid mixing, can be desirable [26] or, on the contrary, undesirable because it can entrain air and damage equipment, particularly pumps, and pose safety problems in nuclear facilities [27–29]. Moreover, as will be illustrated in the following sections, the formation of a vortex has a significant impact on tank emptying and on recirculation systems that use buffer tanks, which drastically affects the emptying time.

Although there exists an extensive literature on bathtub vortices at atmospheric pressure [5,30–46], surprisingly, to the best of our knowledge, no quantitative studies have been investigated on the specific case of emptying a rotating water bottle [7,22].

In this article, we fill this gap and show the many connections that exist between emptying a rotating water bottle and the vortical emptying of open-air tanks. To do so, we perform extensive experimental measurement on a sealed cylindrical tank mounted on a rotating platform. We describe the different stages and regimes that affect the emptying flow and show how the emptying time is affected. We identify three discharge regimes: the first is commonly referred to as the bubble regime,

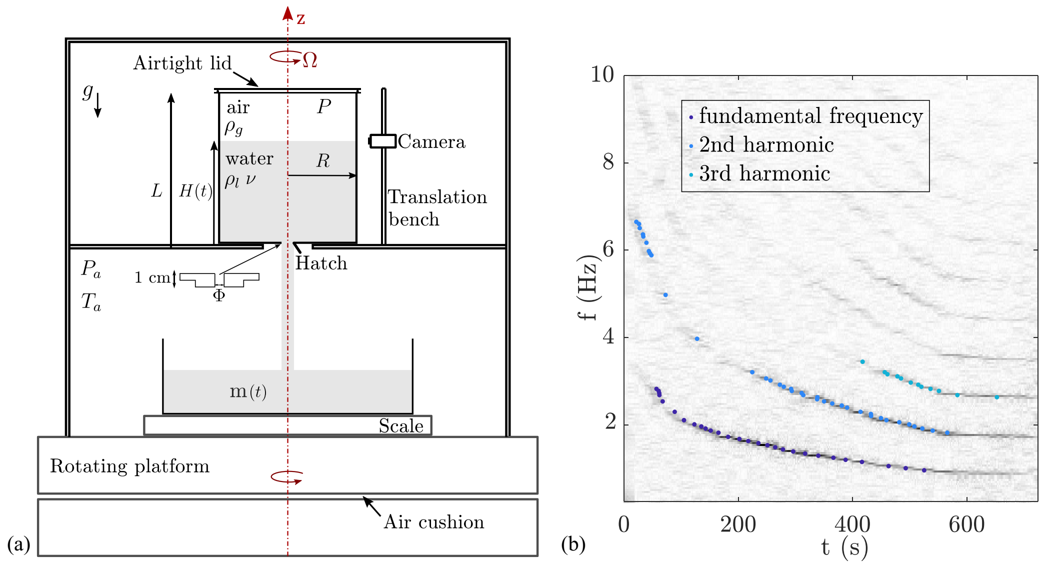

FIG. 1. (a) Schematic drawing of the experimental setup including details of the outlet cylindrical draining pieces. (b) Low-frequency glug-glug sound spectrum as a function of time in the case $\Omega = 0$ rpm and $\Phi = \Phi_1$. The fundamental frequency and its harmonics are marked with dots. The spectrum is obtained by using a sliding Fourier transform processing of the signal.

while the other two involve either a vortical jet or a bathtub vortex. We show how the total draining time depends critically on each of these emptying regimes and their succession.

The article is structured as follows: In Sec. II we present the experimental setup we used to carry out our experiments. Section III presents the effect of rotation on drainage efficiency in terms of the time required for emptying. The three flow regimes identified during rotational emptying are described in Sec. IV and their transition dynamics in Sec. V.

II. EXPERIMENTAL SETUP

The ideal bottle is a Plexiglas cylinder of radius $R = 145 \pm 0.1$ mm and depth $L = 390$ mm. The tank has a rim with a groove designed to accommodate a rubber seal, ensuring a tight seal when the nondeformable lid, made of 1-cm-thick PVC, is closed. The rim and PVC lid of the tank are pierced with 15 evenly spaced holes to accommodate tightening screws, ensuring the proper sealing. It is rigidly mounted on a rotating platform composed of two cylindrical marble plates, each with a diameter of 1.5 m and a thickness of 20 cm. The plates are stacked on top of each other with a 1-mm-thick air cushion in between, such that the upper piece rotate frictionlessly around the vertical axis of rotation Oz, as illustrated in Fig. 1(a). The center of the bottle is aligned with Oz. The rotating velocity Ω can be varied between 0 and 10 rpm. The leveling accuracy has been ensured within ± 0.1 degrees. The bottom plate has a hole drilled in its center for drainage. Two PVC cylindrical draining pieces have been machined [see Fig. 1(a)], each with a thickness of 1 cm and internal hole diameters of $\Phi_1 = 12.7 \pm 0.1$ mm and $\Phi_2 = 19.8 \pm 0.1$ mm, such that $\Phi > 1.9\ell_c$, where $\ell_c = \sqrt{2\sigma/\rho_l g} \approx 3.4$ mm is the capillary length of water in our experiments, in order to avoid the effects of surface tension at the outlet [13]. For diameters below this limit, the emptying time in a tube tends towards infinity [47]. The top surface of each draining piece is flush with the bottom of the tank, and a tight hatch is located beneath it, which can be remotely opened at $t = 0$ s.

At $t = 0$ s, the air at the top of the container is at the atmospheric pressure P_a and both air and water are at the ambient temperature $T_a = 19 \pm 1^\circ$ C. The initial water level is $H_0 = 375 \pm 1$ mm.

The air and chlorinated water used have a specific density ρ_g of 1.2 kg m^{-3} and ρ_l of 998 kg m^{-3}, respectively. The chlorinated water has a kinematic viscosity ν of $(1.03 \pm 0.02) \times 10^{-6}$ m^2 s^{-1} and a surface tension σ of 58 ± 4 mN m^{-1}. This yields an Ekman number $\mathrm{Ek} = \nu/\Omega R^2$ in the range of $4.7 \times 10^{-5} \leqslant \mathrm{Ek} \leqslant 4.7 \times 10^{-4}$.

To ensure that the initial bulk is in solid body rotation, the system is rotated continuously throughout the experiment, beginning one hour before the start of the emptying. The typical spin-up time $H_0/(\nu\Omega)^{1/2}$ [48,49] which holds for cylindrical geometry and in the presence of free surface [50,51] is actually of the order of 10^3 s, smaller than the settling time of 1 h. The initial parabolic deformation of the interface resulting from rotation, which can be expressed as $\Omega^2 R^2/4g$, is in the uncertainty range of H_0, with a magnitude of less than 0.6 mm and thus negligible.

The cumulative mass $m(t)$ of drained water at time t is measured on a digital mass scale with a precision of 0.5 g and a sampling frequency of 7 Hz. No inertial correction is necessary for weight measurements because the force balance is centered on Oz. We determine the water flow rate Q using the time derivative $\dot{m}$ of the measured mass $m(t)$. The average water level $H(t)$ in the tank at time t is computed from $H(t) = H_0 - m(t)/\rho_l \pi R^2$ with an accuracy of 1 mm.

A side view webcam captures the radial profile of the free surface $h(r, t)$. Furthermore, the webcam records the audio throughout the process, allowing us to determine the frequency at which bubbles are formed by analyzing the distinct glug-glug sound they are produced. A typical sound spectrogram is shown in Fig. 1(b). The spectrum is obtained by using a sliding Fourier transform processing of the signal. The fundamental frequency and its harmonics obtained by considering the maximum intensity of the spectrum are marked with dots and allow us to deduce the associated period τ.

To study the reproducibility of the experiments, some of them were replicated under identical conditions. The experiments with diameter Φ_1 were repeated eight and seven times at $\Omega = 4$ and 5 rpm, respectively. For these rotations speed, the draining velocity can undergo different trends, with a nonreproducible appearance of the different regimes (a point that will be addressed in the final part of this article). For all the other rotation speeds, the standard deviation of the draining time is below 2% for large Ω and diameter Φ_1, and 5% for diameter Φ_2. For smaller Ω, the standard deviation is below 5% for diameter Φ_1 and 7% for diameter Φ_2.

III. THE EFFECT OF ROTATION ON DRAINAGE EFFICIENCY

We explore the relationship between the emptying time T_e of the sealed tank and the rotating velocity Ω of the platform. The emptying time T_e is defined as the time it takes for 99% of the initial water level to drain. In this context, efficiency is defined as the ratio of the emptying time T_e with rotation to that without rotation, the smaller the ratio, the more efficient the drain. Figure 2(a) illustrates the scaled emptying time $T_e(\Omega)/T_e(0)$ as a function of the platform's rotating velocity Ω, where $T_e(0)$ is the emptying time in the absence of rotation. The time values shown are averaged over the number of experiments performed for each rotation. They have also been doubled for diameter Φ_1 and $\Omega = 4$ and 5 rpm, where emptying can follow different behaviors, leading to drastically different emptying times, as will be explained in Sec. V. For both outlet sections, an increase in the rotating velocity of the tank initially leads to a reduction in the emptying time. The shortest emptying time is observed at the optimal rotating velocities $\Omega_{\mathrm{opt}}(\Phi_1) = 4.0 \pm 0.5$ rpm and $\Omega_{\mathrm{opt}}(\Phi_2) = 3.0 \pm 0.5$ rpm for sections Φ_1 and Φ_2, respectively. However, this minimum time is not reproducible. For section Φ_1, the emptying time can be much longer for intermediate values of the rotational speed, namely, 4 and 5 rpm. Nonreproducible emptying times are also expected at $\Omega = 4$ rpm for diameter ϕ_2, as will be justified in Sec. V. Further increasing the tank's rotation increases the discharge time, which follows a seemingly linear trend whose slope depends on the outlet diameter Φ, as shown by the blue dashed lines in Fig. 2(a). Notably, when plotting the scaled emptying time as a function of the dimensionless parameter $\Omega(\Phi/2)^2/\nu = (\Phi/2R)^2\mathrm{Ek}^{-1}$ [Fig. 2(b)], the points collapse on a master line. This dimensionless parameter is thus the relevant control parameter for describing the bathtub vortex emptying process that occurs when the rotation

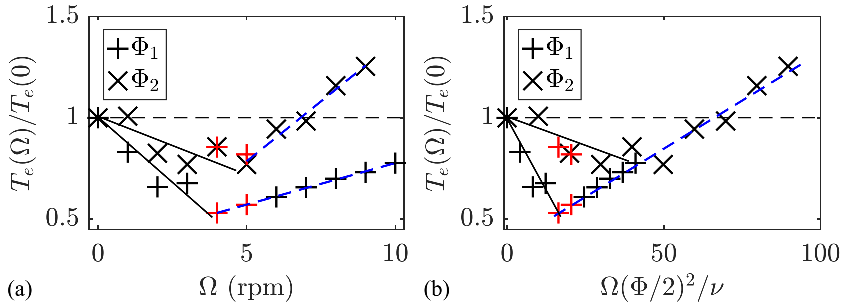

FIG. 2. Emptying time $T_e(\Omega)$ scaled by the emptying time without rotation $T_e(0)$ (a) as a function of the rotating velocity Ω, and (b) as a function of $\Omega(\Phi/2)^2/\nu$. The black horizontal dashed lines represent the nonrotating case ($\Omega = 0$ rpm). The black solid lines are included as a visual guide of the dispersion of the results for intermediate Ω. The blue dashed lines represent the linear fit of the experiments for which only regimes 2 and 3 are significant during drainage. The estimated standard deviation across different measurements is included in the size of the points, except for Φ_1 and $\Omega = 4$ and 5 rpm, points for which the two observed behaviors are shown in red.

is large enough (see Sec. IV), as reported in Ref. [5]. When the rotation speed Ω becomes sufficiently large, the bathtub vortex regime becomes dominant and has time to establish. The trend (blue dashed line) in Fig. 2(b) can differ for sections with smaller diameters, where surface tension has a considerable effect on the flow, potentially even stopping it, and can differ also for sections that are too large, as the tank would then empty too quickly and the short draining time would not allow the vortex to establish properly. It is worth noting that, for the smaller outlet diameter Φ_1, the emptying time remains shorter than the one of the nonrotating case even at the highest rotating velocity tested in our experimental setup. However, for the larger section Φ_2, the discharge time exceeds that of the nonrotating case once Ω exceeds 8 rpm. Contrary to a common assumption, our results reveal that rotating the tank does not always result in faster emptying compared with the nonrotating case. Instead, we identify an optimal tank rotating velocity Ω_{opt} that maximizes the efficiency of the emptying process.

To delve further, we analyze the behavior of the scaled water height H/H_0 inside the container as a function of the dimensionless time $t/T_e(0)$ [see Figs. 3(a) and 3(b) for sections Φ_1 and Φ_2, respectively]. Different emptying trends related to different regimes (see Sec. IV for a detailed description) are observed depending on the rotating velocity of the system.

At low rotating velocities ($\Omega \leqslant 1$ rpm), the evolution of H/H_0 follows a nearly linear trend with time. This evolution is characteristic of a nonrotating regime in which bubbles periodically form in the system, which we refer to as regime 1 or bubble regime (dotted lines). At higher rotating velocities [$\Omega(\Phi_1) \geqslant 4$ rpm and $\Omega(\Phi_2) \geqslant 5$ rpm], while the duration of regime 1 becomes negligible compared with the emptying time, two other regimes are observed, namely, the vortical jet regime and the bathtub vortex regime, labeled as regimes 2 (dashed lines) and 3 (solid lines), respectively. In regime 2, the height decreases at a faster rate compared with regime 1, following here also a nearly linear trend. In regime 3, a nonlinear decrease in height is observed, characteristic of the discharge behavior in rotating free-surface tanks (see Sec. IV for further explanations). As can be seen in Fig. 3, this nonlinear decay can become less effective than the linear decay of regime 1, which explains why the emptying becomes less effective when Ω is too large and regime 3 dominates. At intermediate rotating velocities ($2 \leqslant \Omega(\Phi_1) \leqslant 3$ rpm and $2 \leqslant \Omega(\Phi_2) \leqslant 4$ rpm), all three regimes are observed sequentially. The relative duration of each regime during an experiment influence the overall effectiveness of the drainage process.

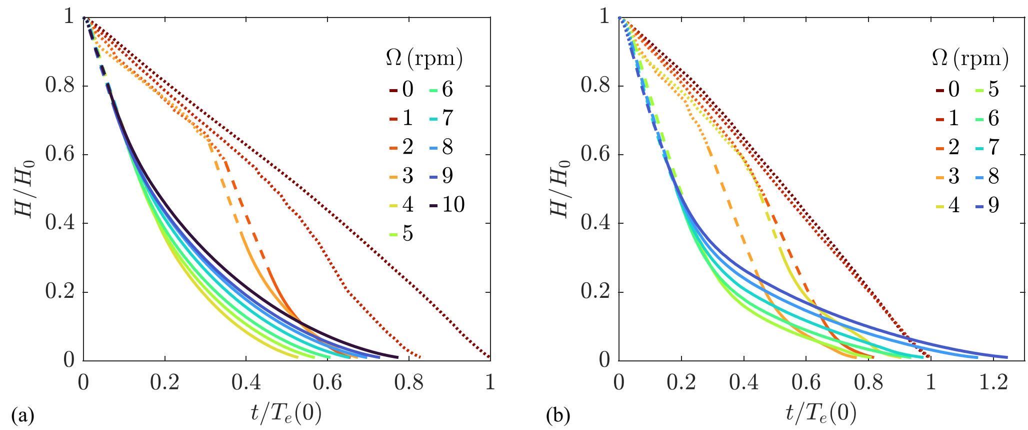

FIG. 3. (a) Time evolution of H/H_0 for Φ_1 and (b) for Φ_2 at $0 \leqslant \Omega \leqslant 10$ rpm. Dotted lines indicate the presence of regime 1, dashed lines indicate the presence of regime 2, and solid lines indicate the presence of regime 3. The time t is scaled by the emptying time $T_e(0)$ when $\Omega = 0$ rpm. For high rotation speeds, regime 1 only lasts between 5% and 6% of the drainage time.

IV. CHARACTERIZATION OF THE THREE DIFFERENT EMPTYING REGIMES

The bubble regime (regime 1) represents the discharge regime observed in the absence of rotation [see Fig. 4(a) at $t/T_e(\Omega) = 0.01$]. It is characterized by the cyclic occurrence of air bubbles at the outlet of the tank, which rise by buoyancy up to the top of the tank. Air is therefore gradually replacing water in the upper portion of the tank, with a decreasing frequency over time, as shown in Figs. 1(b) and 5. The analytical expression proposed by Clanet and Searby [13] for the period of bubble formation is applicable to containers whose aspect ratios allow the inertia term $(2R/\Phi)^4 {v_Q}^2$ to be neglected. This does not apply to our experiments [13]. Figure 5 shows the scaled bubble periods $\tau/T_e(0)$ measured for different rotating velocities. The period of the glug-glug is clearly related to H/H_0, whereas it depends only slightly on Ω over the explored range of Φ and Ω. The bubble regime is characterized by an oscillating draining velocity whose mean value remains constant over time and relatively small compared with the other two regimes, as shown in Fig. 4(b). The emptying velocity in this regime can be modeled using Whalley's approach [20] as $v_B = C^2\sqrt{g\Phi(\rho_l - \rho_g)}/(\rho_g^{1/4} + \rho_l^{1/4})^2$, with $C \approx 0.916$ as proposed by Kordestani and Kubie [10]. The draining velocity obtained from this model ($v_B = 0.261$ m s^{-1}) is in relatively good agreement with the experimentally measured mean velocity ($v_{QB} = 0.276$ m s^{-1}) for the case $\Omega = 0$ rpm and $\Phi = \Phi_2$ (Φ_1 is not in the range of previous studies). Intermittent bursts can be observed in Fig. 4(b) (black arrows), see also the Supplemental Material [52], when regime 2 transiently settles in the bubble regime, for $\Omega > 0$.

Regime 2 is characterized by a highly unsteady vortical jet flow. This regime occurs when vorticity concentrates along the discharge axis aligned with Oz. However, the generated vortex is not strong enough to maintain a continuous gaseous core from the outlet to the free surface. Instead, it takes the form of an "air jet," as shown in Fig. 4(a) at $t/T_e(\Omega) = 0.53$. In this regime, the fluid continuously flows through the discharge section. The pressure in the air volume is lower than the atmospheric pressure P_a, but larger than in regime 1 (see Sec. V for further explanations). This difference in pressure explains why regime 2 is more effective than regime 1 in draining, as seen in Fig. 4(b), where the draining velocity is the largest and exhibits only slight variations with H/H_0.

Regime 3 is similar to the bathtub vortex regime observed in rotating free-surface tanks [30,31,34–46] in terms of interface deformation [see Fig. 4(a) at $t/T_e(\Omega) = 0.68$], as well as draining velocity. In Fig. 6(a), we compared experiments with and without a lid for a rotation rate of $\Omega = 5$ rpm. The red curve, representing the standard case with a lid, matches perfectly with the

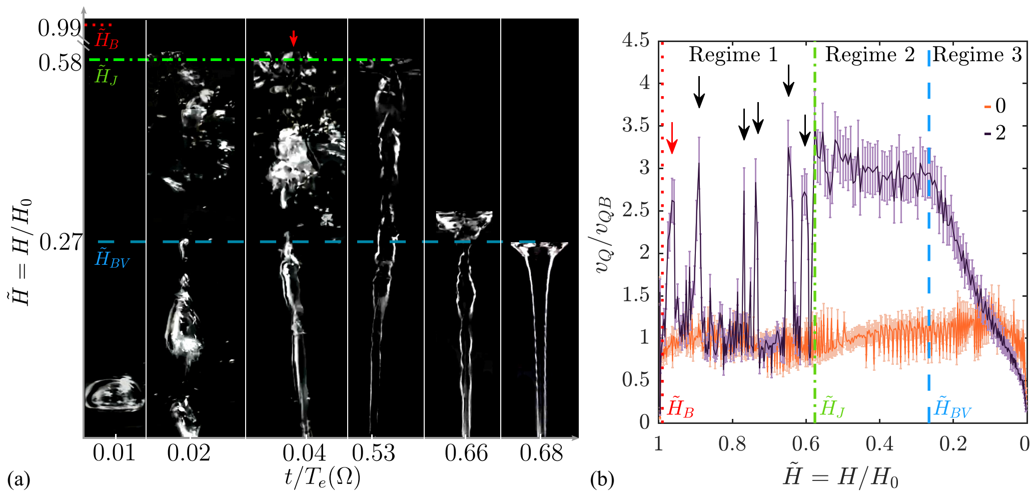

FIG. 4. (a) Sequence of photographs for the case $\Omega = 2$ rpm and Φ_1. The first bubble appears after $t/T_e(\Omega) = 0.01$ with a normalized water height $\tilde{H} = \tilde{H}_B$ (out of scale). Regime 2 stabilizes at $t/T_e(\Omega) = 0.53$, with a normalized water height $\tilde{H} = \tilde{H}_J$. Regime 3 stabilizes at $t/T_e(\Omega) = 0.68$, with a normalized water height $\tilde{H} = \tilde{H}_{BV}$. Images capturing the interfacial aspect during the transitions between regimes 1 and 2 and between regimes 2 and 3 were taken at $t/T_e(\Omega) = 0.02$ and $t/T_e(\Omega) = 0.66$, respectively. At $t/T_e(\Omega) = 0.04$ (red arrow), the first appearance of the unstable vortical jet (regime 2) is observed, as also shown in panel (b). (b) Draining velocity v_Q normalized by the mean velocity of the case without rotation v_{QB}, plotted for $\Omega = 0$ rpm and $\Omega = 2$ rpm with section Φ_1 as a function of H/H_0. The boundaries of the different regimes $\tilde{H} = \tilde{H}_B, \tilde{H}_J, \tilde{H}_{BV}$ for the $\Omega = 2$ rpm case are represented respectively by dotted lines, dotted-dashed lines and dashed lines, matching the color scheme used in panel (a). Arrows on the velocity curve indicate the appearances of the jet, which coincide with the measured velocity peaks. The first arrow in red corresponds to the photographic image marked by a red arrow in panel (a).

gray dashed curve of the lidless case from a critical height $H/H_0 = 0.46$, which is lower than the height at which regime 3 establishes ($H/H_0 = 0.6$). The vortex regimes in both configurations are thus identical once the vortex is well established. Furthermore, the draining velocity v_Q normalized by the classical Torricelli velocity $v_T = \beta\sqrt{2gH}$ is shown in Figs. 6(b) and 6(c) as a function of the water depth H/H_0 at $\Omega = 7$ rpm for both sections. The dashed lines $v_Q/v_T = 1$ serve as a reference to illustrate Torricelli's law. It can be observed that the measured draining velocity is significantly lower than the classical Torricelli case. Following Caquas *et al.* [5], the draining velocity v_{BV} in the presence of a bathtub vortex can be predicted (red data points in Fig. 6) based on the shape of the free surface as

$$v_{BV}(t) = \beta\sqrt{\frac{4g}{(\Phi/2)^2}\int_0^{\Phi/2} h(r,t)r dr}, \tag{1}$$

with a correction coefficient $\beta \approx 0.6$, consistent with values reported in the literature for a circular hole [2,13]. This agreement demonstrates that once the vortex is formed, the draining velocity v_Q, is no longer influenced by the presence of the tank lid nor subject to hysteresis effects. Thus, in this regime, the top and bottom of the tank are continuously connected through the gaseous core. Consequently, air pressure above the water volume is P_a. In this regime, the larger the rotating velocity of the platform, the faster the draining velocity decreases as the water level decreases. This can be attributed to the expansion of the gaseous core with increasing rotation, resulting in a reduced average water height above the outlet section and a reduced wet section at the outlet. In contrast, in

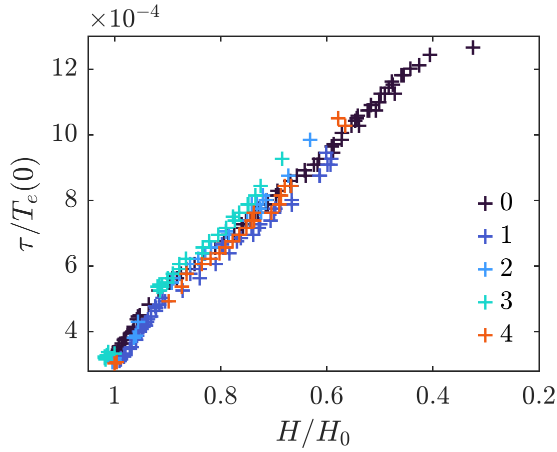

FIG. 5. Period of bubble appearance τ scaled by the emptying time without rotation $T_e(0)$ for different rotating velocities as a function of the scaled water height H/H_0 for section Φ_1.

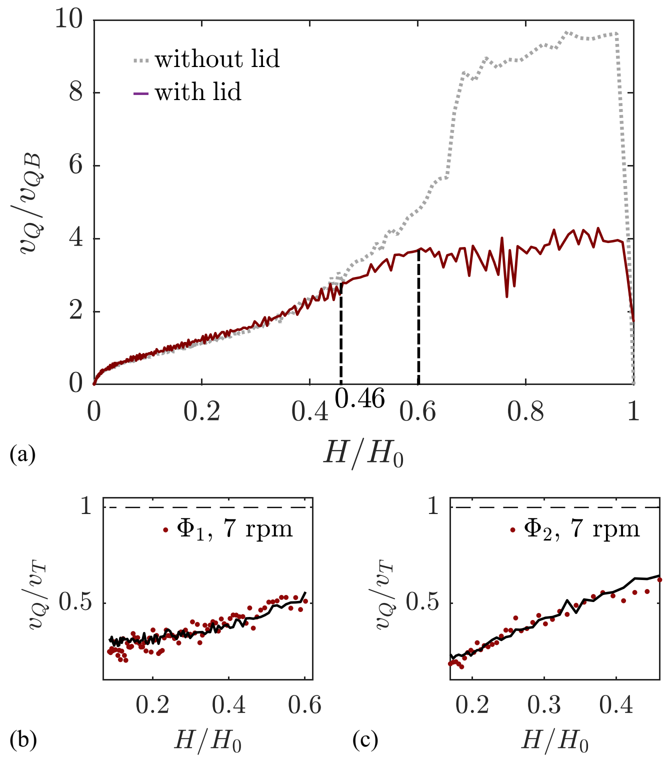

FIG. 6. (a) Draining velocity v_Q scaled by v_{QB} as a function of the instantaneous water height H scaled by its initial value H_0 for the case Φ_1 at $\Omega = 5$ rpm. The red curve represents the standard experiment with the airtight lid, while the gray dotted line represents the case without lid (i.e., at atmospheric pressure throughout the experiment). (b), (c) Draining velocity v_Q scaled by v_T as a function of the instantaneous water height H scaled by its initial value H_0 for (b) Φ_1 and $\Omega = 7$ rpm, and (c) Φ_2 and $\Omega = 7$ rpm. The solid black lines correspond to mass measurements and the red points to Eq. (1) with interface shape measurements. The black dashed line shows the reference value $v_Q = v_T$. Here, the estimated value of the corrected coefficient β is approximately 0.6.

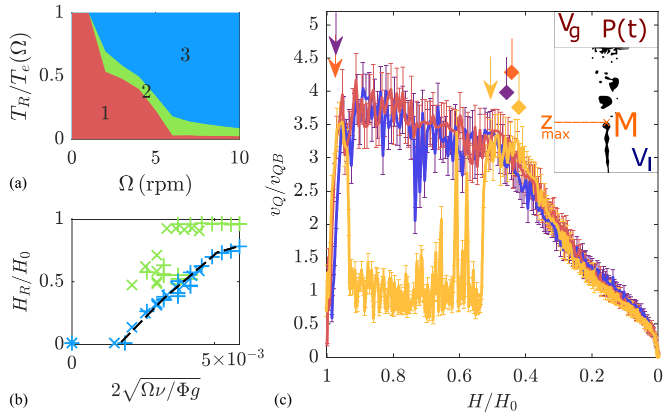

FIG. 7. (a) Diagram showing the occurrence of the different regimes as a function of the mean scaled regime time $T_R/T_e(\Omega)$ and the rotating velocity Ω for section Φ_1. Regime 1 appears in red, regime 2 in green and regime 3 in blue. (b) Normalized height H_R/H_0 at which each regime appears plotted against $2\sqrt{\Omega\nu/\Phi g}$ for the two sections. The appearance of regime 2 ($H_R = H_J$) is indicated in green, while the appearance of regime 3 ($H_R = H_{BV}$) is indicated in blue. All experiments for which the onset of regime 2 differ are represented. The black dashed lines are included as a visual guide. (c) Scaled draining velocities v_Q/v_T at the threshold value for $\Omega = 4$ rpm and section Φ_1. For this threshold value of Ω, the results of three emptying, in the same initial configuration, are shown, and show different trends. The onset of the jet regime is marked with arrows, and the transition to the vortex regime is indicated by diamonds. The colors of the symbols correspond to those of the curves. The inset shows the schematic diagram of the experiment.

regime 2, the radius of the gaseous core remains small and relatively constant throughout the entire regime. Ultimately, regime 3 becomes even less effective than regime 1.

V. DYNAMICS OF TRANSITIONS

As mentioned in Sec. III, the efficiency of the draining process, as a function of the rotating velocity, is highly dependent on the relative duration of each of the three emptying regimes described in the previous section. The transition between the different regimes is not straightforward either, particularly given the unstable nature of regime 2. To describe the transitions between each of the three draining regimes, we consider the case of Fig. 4 where $\Omega = 2$ rpm and $\Phi = \Phi_1$. The visualization of transitions between different regimes [see Fig. 4(a)] is also indicated in Fig. 4(b), corresponding to the changes in slope of the velocity curve.

At $t/T_e(\Omega) = 0$, the draining is initiated at the pressure P of the air volume V_g located in the upper zone of the tank [see inset of Fig. 7(c)], which is initially equal to the atmospheric pressure P_a. The fluid flows until the pressure P reaches the critical value $P_c = P_a - \rho_l g H$. Once this pressure is reached, the external air at the outlet pushes the water, forming a bubble. This bubble grows, expanding both the volume of water V_l (V_l being the volume of water including bubbles or air jet) and the pressure P of the air volume V_g. At $t/T_e(\Omega) = 0.01$, the bubble pinches off and detaches from the outlet. The tank drains and P decreases again. When the pressure P reaches the new $P_c(H)$, a second bubble forms at the outlet. Eventually, by repeating the aforementioned mechanism [17], bubbles form periodically in the tank. For larger outlet diameters (such as Φ_2), counter-currents of water can occur when a bubble is formed [22].

As the container drains, vorticity concentrates and the pressure decreases along the Oz axis. From the start of the draining [see Fig. 4(a) at $t/T_e(\Omega) = 0.02$], the resulting stretching can cause the rising bubbles to elongate. Once the stretching reaches a critical intensity, it can lead to the formation of an air jet, which, due to the inherent instability of the vortex, can subsequently disappear [see Fig. 4(a) at $t/T_e(\Omega) = 0.04$]. Before reaching the surface, the jet breaks up into bubbles at a level $z_{\max} < H$ [see inset of Fig. 7(c)]. The pressure $P(t)$ at point M, which belongs to the air core at height $z_{\max}$, must satisfy $P_a = P(t) + \rho_l g[H(t) - z_{\max}]$, where $z_{\max}$ increases as the vortex becomes stronger.

When $H_B \leqslant H < H_J$ [see Fig. 4(b)], regime 1 dominates, the vortex is weak, the height $z_{\max}$ is small, and the pressure P approaches the previous critical value P_c. The air jet can even disappear at the critical value $P(t) = P_c$. In this case, there is no more outflow, which breaks the structure of the vortex, and regime 1 reappears. Generally, the intermittent bursts of regime 2 are brief ($t \approx 4$ s) and only represents a small fraction of regime 1. It can be observed in Fig. 4(b) where peaks of draining velocity correspond to the appearance of the intermittent air jet.

When $H_J < H < H_{BV}$ [see Fig. 4(b)], regime 2 stabilizes and the air jet reaches a height $z_{\max}$ close to the interface. The airflow brought by the jet is sufficient for the pressure P to increase. When the pressure $P(t)$ approaches P_a, the transition from regime 2 to regime 3 initiates. Simultaneously, the upper interface undergoes deformation in an attempt to match the shape of the air jet. This transition can occur continuously, as showed in the case of $\Omega = 2$ rpm presented in Fig. 4(a) at $t/T_e(\Omega) = 0.66$. In this scenario, the interface deformation exhibits a hybrid form, combining characteristics of both an air jet and the typical deformation observed in a bathtub vortex interface. However, for higher rotating velocities (see the Supplemental Material [53]), the transition can become oscillatory. In such cases, the air jet can intermittently disappear when the pressure $P(t)$ is high, while a distinctive bathtub vortex deformation appears at the upper air-water interface. If the vortex intensity is insufficient for the interface deformation to rapidly extend into the outlet section, the pressure $P(t)$ decreases once again, causing the jet to reappear. The interface deformation then oscillates between these two states in a pulsating cycle until the pressure equilibrates at $P(t) = P_a$.

The transitions between the successive regimes, and therefore the time spent in each of them, directly depend on the vortex intensity, and thus on Ω. Figure 7(a) shows the diagram of occurrences of the different regimes. The duration of regime 1 decreases with increasing Ω. For high rotation velocities, the vortex establishes itself rapidly and remains stable, causing regime 1 to last only a few seconds. Consequently, its influence on the emptying process is negligible. On the contrary, regime 3 behaves in the opposite manner. Its duration decreases as Ω decreases, and for low values of Ω, regime 3 does not occur at all.

The swirl ratio $S = \Omega\Phi/U$ [31], commonly used in tornado research to analyze their intensity and stability [54], is defined locally at the discharge section. Here, $U = 2Q/\pi\delta\Phi$ represents the characteristic radial velocity in the Ekman layer at the bottom of the tank [43] during the early stages of the emptying process. During this stage, Q is approximately equal to $\sqrt{\Phi g}(\Phi/2)^2$, resulting in the simplification of the swirl ratio to $S = 2\sqrt{\Omega\nu/\Phi g}$. Figure 7(b) illustrates the heights at which the jet regime H_J (in green) and the bathtub vortex regime H_{BV} (in blue) occur as a function of $2\sqrt{\Omega\nu/\Phi g}$. The evolution of H_{BV} exhibits a seemingly linear increase with the swirl ratio within the range of tested Ω values (it is expected that the ratio H/H_0 approaches 1 for higher Ω values). The occurrence of the stable vortex regime is therefore clearly correlated to the initial swirl ratio. This transition point between regime 2 and 3 is also reproducible [see Figs. 7(b) and 7(c)].

The establishment of regime 2 requires a vortex and therefore a sufficient Ω, but the vortex must not be too intense in order to delay the transition to regime 3. Thus, the fraction of time spent in regime 2 first increases with Ω, becomes maximal for an optimal rotating velocity Ω_J which depends on Φ and decreases for larger values of Ω.

At the largest Ω, the water level H_J at which the transition occurs between regime 1 and 2 is repeatable and appears to be constant [see Fig. 7(b)]. The value of the plateau varies very slightly with the diameter Φ, with $H_J(\Phi_1)/H_0 = 0.96 \pm 0.01$ and $H_J(\Phi_2)/H_0 = 0.92 \pm 0.01$. However, this is no longer true for intermediate and small Ω. The values of H_J become random. Figure 7(c) shows the draining velocity for several experiments with the same settings ($\Omega = 4$ rpm and Φ_1). The red and purple curves exhibit a behavior typical at large Ω, with mainly regime 2 and 3 only present. The yellow curve is representative of a case where all three regimes are successively present, as is usually observed at intermediate Ω. Across all experiments conducted at $\Omega = 4$ and 5 rpm with diameter Φ_1, we observed that approximately half of the curves followed either an intermediate rotation trend or a high rotation trend. This phenomenon was not observed for diameter Φ_2, but the few experiments carried out (4 at $\Omega = 4$ rpm, 3 at $\Omega = 5$) do not allow us to draw any general conclusions about this case.

Similarly to the jet intermittence in regime 1, the unpredictability of the settling of regime 2 underlines the instability of the vortex in regime 2. This explains why the fastest emptying is not always obtained for a repeatable value of Ω.

VI. CONCLUSIONS

Our study has demonstrated that the draining of a closed vessel in a rotating frame is far from being trivial, with three successive regimes identified whose occurrence and duration depend on Ω, H, and Φ. We found that rotation is efficient to empty the tank only when an optimal rotating velocity Ω_{opt} is reached. In our range of studied diameters and rotations, we observed that the draining time increases almost linearly with the parameter $\Omega(\Phi/2)^2/\nu$ once the critical value Ω_{opt} is reached. By studying the critical heights at which the regimes occur, we noticed that the critical height for the occurrence of regime 2 is not well defined and nonreproducible at low values of Ω, but becomes reproducible and constant beyond Ω_{opt}. As for the height H_{BV}, it can be expressed in terms of the swirl ratio $S = 2\sqrt{\Omega\nu/g\Phi}$ and scales almost linearly over the range of explored Ω values.

Although idealized, our experiment provides a better understanding of the emptying of a rotating water bottle. The chosen ratio H_0/R in our experiment is approximately three times smaller than that of a typical water bottle, while H_0 is of the same order of magnitude. Variations in this aspect ratio should not change the physics of the emptying process. It is worth noting that while the water height does not affect the velocity during the bubble regime, the draining velocity will be larger for a larger height as soon as the vortex is present. Therefore, for an equivalent water volume, a higher H_0/R ratio leads to a shorter emptying time. The choice of a larger radius R allows for a slower emptying rate and longer visualization of the different regimes compared with a typical water bottle. The ratio Φ/R also is chosen to be very small in our case to remain within the typical approximation used for the Torricelli's law. For larger aspect ratios, as in the case of a typical water bottle ($\Phi/R \approx 0.2$), we expect a modification in the draining velocity expressed by Eq. (1), as the interface velocity would no longer be negligible in the balance. However, for aspect ratios close to those of a bottle, the three regimes mentioned in this article can be observed. Only the duration of each regime is affected.

[1] E. Torricelli, *Opera Geometrica [De sphera et Solidis Spharalibus; De Motu Gravium; De Dimensione Parabolae]* (Amadoro Massa & Lorenzo de Landis, Florence, 1644).

[2] G. K. Batchelor, *An Introduction to Fluid Dynamics* (Cambridge University Press, 1967).

[3] C. Clanet, Clepsydrae, from Galilei to Torricelli, Phys. Fluids **12**, 2743 (2000).

[4] J. Ferrand, L. Favreau, S. Joubaud, and E. Freyssingeas, Wetting effect on Torricelli's law, Phys. Rev. Lett. **117**, 248002 (2016).

[5] A. Caquas, L. R. Pastur, A. Genty, and P. Gondret, Bathtub vortex effect on Torricelli's law, Phys. Rev. Fluids **8**, 044702 (2023).

[6] P. B. Whalley, Two-phase flow during filling and emptying of bottles, Int. J. Multiphase Flow **17**, 145 (1991).

[7] H. C. Mayer, Bottle emptying: A fluid mechanics and measurements exercise for engineering undergraduate students, Fluids **4**, 183 (2019).

[8] L. Rohilla and A. K. Das, Fluidics in an emptying bottle during breaking and making of interacting interfaces, Phys. Fluids **32**, 042102 (2020).

[9] F. Geiger, K. Velten, and F.-J. Methner, 3D CFD simulation of bottle emptying processes, J. Food Eng. **109**, 609 (2012).

[10] S. S. Kordestani and J. Kubie, Outflow of liquids from single-outlet vessels, Int. J. Multiphase Flow **22**, 1023 (1996).

[11] S. Tang and J. Kubie, Further investigation of flow in single inlet/outlet vessels, Int. J. Multiphase Flow **23**, 809 (1997).

[12] O. Schmidt and J. Kubie, An experimental investigation of outflow of liquids from single-outlet vessels, Int. J. Multiphase Flow **21**, 1163 (1995).

[13] C. Clanet and G. Searby, On the glug-glug of ideal bottles, J. Fluid Mech. **510**, 145 (2004).

[14] P. Héraud, Étude de la dynamique des bulles infinies: application à l'étude de la vidange et du remplissage de réservoir, Ph.D. thesis, Université de Provence-Aix-Marseille I, 2002.

[15] S. Mer, O. Praud, J. Magnaudet, and V. Roig, Simulating the emptying of a water bottle with a multi-scale two-fluid approach, in *ASME 2018 5th Joint US-European Fluids Engineering Division Summer Meeting*, Vol. 51579 (American Society of Mechanical Engineers Digital Collection, 2018), Paper No. FEDSM2018-83196, V003T18A004.

[16] S. Mer, O. Praud, J. Magnaudet, and V. Roig, Emptying of a bottle: How a robust pressure-driven oscillator coexists with complex two-phase flow dynamics, Int. J. Multiphase Flow **118**, 23 (2019).

[17] A. A. K. Tehrani, M. A. Patrick, and A. A. Wragg, Dynamic fluid flow behaviour of a tank draining through a vertical tube, Int. J. Multiphase Flow **18**, 977 (1992).

[18] A. Tehrani, A. Wragg, and M. Patrick, How fast will your bottle empty?, in *Proceedings of the ICHEME, London* (Institution of Chemical Engineers, 1994), pp.1069–1071.

[19] J. Liang, Y. Ma, and Y. Zheng, Characteristics of air-water flow in an emptying tank under different conditions, Theor. Appl. Mech. Lett. **11**, 100300 (2021).

[20] P. B. Whalley, Flooding, slugging and bottle emptying, Int. J. Multiphase Flow **13**, 723 (1987).

[21] C. Schwefler, P. Nienaber, and H. C. Mayer, The emptying of a perforated bottle: Influence of perforation size on emptying time and the physical nature of the process, Fluids **8**, 225 (2023).

[22] M. I. Kohira, N. Magome, H. Kitahata, and K. Yoshikawa, Plastic bottle oscillator: Rhythmicity and mode bifurcation of fluid flow, Am. J. Phys. **75**, 893 (2007).

[23] M. I. Kohira, H. Kitahata, N. Magome, and K. Yoshikawa, Plastic bottle oscillator as an on-off-type oscillator: Experiments, modeling, and stability analyses of single and coupled systems, Phys. Rev. E **85**, 026204 (2012).

[24] J. Jia, Z. Shangguan, H. Li, Y. Wu, W. Liu, J. Xiao, and J. Kurths, Experimental and modeling analysis of asymmetrical on-off oscillation in coupled non-identical inverted bottle oscillators, Chaos **26**, 116301 (2016).

[25] E. D. Schneider and D. Sagan, *Into the Cool: Energy Flow, Thermodynamics, and Life* (University of Chicago Press, Chicago, 2005).

[26] D. Kim and D. Kim, Free-surface vortex formation and aeration by a submerged rotating disk, Chem. Eng. Sci. **243**, 116787 (2021).

[27] D. Tenchine, C. Fournier, and Y. Dolias, Gas entrainment issues in sodium cooled fast reactors, Nucl. Eng. Des. **270**, 302 (2014).

[28] B. Moudjed, J. Excoffon, R. Riva, and L. Rossi, Experimental study of gas entrainment from surface swirl, Nucl. Eng. Des. **310**, 351 (2016).

[29] H. Bhatia, U. Bieder, and D. Guenadou, Rankine-vortex model based assessment of CFD methods for simulating the effect of gas entrainment observed in the hot-pool of sodium coold fast breeder reactors, Prog. Nucl. Energy **137**, 103794 (2021).

[30] H. A. Einstein and H. Li, Steady vortex flow in a real fluid, in *Proceedings of the Heat Transfer and Fluid Mechanics Institute* (Stanford University Press, 1951), pp. 33–43.

[31] W. S. Lewellen, A solution for three-dimensional vortex flows with strong circulation, J. Fluid Mech. **14**, 420 (1962).

[32] A. H. Shapiro, Bath-tub vortex, Nature (London) **196**, 1080 (1962).

[33] L. M. Trefethen, R. W. Bilger, P. T. Fink, R. E. Luxton, and R. I. Tanner, The bath-tub vortex in the southern hemisphere, Nature (London) **207**, 1084 (1965).

[34] H. J. Lugt, *Vortex Flow in Nature and Technology* (Wiley-Interscience, New York, 1983), p. 305.

[35] L. K. Forbes and G. C. Hocking, The bath-plug vortex, J. Fluid Mech. **284**, 43 (1995).

[36] Y. A. Stepanyants and G. H. Yeoh, Burgers–Rott vortices with surface tension, Z. Angew. Math. Phys. **59**, 1057 (2008).
[37] S. Shingubara, K. Hagiwara, R. Fukushima, and T. Kawakubo, Vortices around a sinkhole: Phase diagram for one-celled and two-celled vortices, J. Phys. Soc. Jpn. **57**, 88 (1988).
[38] L. Bøhling, A. Andersen, and D. Fabre, Structure of a steady drain-hole vortex in a viscous fluid, J. Fluid Mech. **656**, 177 (2010).
[39] T. S. Lundgren, The vortical flow above the drain-hole in a rotating vessel, J. Fluid Mech. **155**, 381 (1985).
[40] P. A. Tyvand and K. B. Haugen, An impulsive bathtub vortex, Phys. Fluids **17**, 062105 (2005).
[41] Y. A. Stepanyants and G. H. Yeoh, Stationary bathtub vortices and a critical regime of liquid discharge, J. Fluid Mech. **604**, 77 (2008).
[42] A. Andersen, T. Bohr, B. Stenum, J. J. Rasmussen, and B. Lautrup, Anatomy of a bathtub vortex, Phys. Rev. Lett. **91**, 104502 (2003).
[43] A. Andersen, T. Bohr, B. Stenum, J. J. Rasmussen, and B. Lautrup, The bathtub vortex in a rotating container, J. Fluid Mech. **556**, 121 (2006).
[44] K. Ito, T. Ezure, and H. Ohshima, Development of vor-tex model with realistic axial velocity distribution, The Japan Soc. Mech. Eng. **80**, 1 (2014).
[45] A. Duinmeijer, G. Oldenziel, and F. Clemens, Experimental study on the 3D-flow field of a free-surface vortex using stereo PIV, J. Hydraul. Res. **58**, 105 (2020).
[46] Y. Recoquillon, Étude expérimentale et numérique des écoulements diphasiques dans la boîte à eau d'un véhicule automobile, Ph.D. thesis, Université d'Orléans, 2013.
[47] E. E. Zukoski, Influence of viscosity, surface tension, and inclination angle on motion of long bubbles in closed tubes, J. Fluid Mech. **25**, 821 (1966).
[48] H. P. Greenspan and L. N. Howard, On a time-dependent motion of a rotating fluid, J. Fluid Mech. **17**, 385 (1963).
[49] P. W. Duck and M. R. Foster, Spin-up of homogeneous and stratified fluids, Annu. Rev. Fluid Mech. **33**, 231 (2001).
[50] Y.-C. Chen, S.-L. Huang, Z.-Y. Li, C.-C. Chang, and C.-C. Chu, A bathtub vortex under the influence of a protruding cylinder in a rotating tank, J. Fluid Mech. **733**, 134 (2013).
[51] W. Yang, I. Delbende, Y. Fraigneau, and L. M. Witkowski, Large axisymmetric surface deformation and dewetting in the flow above a rotating disk in a cylindrical tank: Spin-up and permanent regimes, Phys. Rev. Fluids **5**, 044801 (2020).
[52] See the Supplemental Material at http://link.aps.org/supplemental/10.1103/PhysRevFluids.9.064701 for a video on the intermittency of regime 2 at 3 rpm for section Φ_1.
[53] See Supplemental Material at http://link.aps.org/supplemental/10.1103/PhysRevFluids.9.064701 for a video of the transition between regime 2 and 3 at 9 rpm for section Φ_1.
[54] D. C. Lewellen, W. S. Lewellen, and J. Xia, The influence of a local swirl ratio on tornado intensification near the surface, J. Atmos. Sci. **57**, 527 (2000).